Computing first-arrival seismic traveltimes on unstructured 3-D tetrahedral grids using the Fast Marching Method

Peter G. Lelièvre, Colin G. Farquharson and Charles A. Hurich

Memorial University of Newfoundland, St. John's, Newfoundland, Canada. E-mail: plelievre@mun.ca

SUMMARY

The Fast Marching Method is an efficient numerical algorithm for propagating interfaces such as first-arrival seismic wave fronts travelling through a velocity distribution. Fast Marching solutions have been developed for use on rectilinear grids in 2-D and 3-D. We are interested in unstructured grids as they provide some computational advantages when dealing with complicated shapes that are difficult to represent with rectilinear grids. Fast Marching solutions have also been developed for unstructured 2-D triangular grids but this has yet to be extended to unstructured 3-D tetrahedral grids. In this paper, we extend the Fast Marching Method to unstructured 3-D tetrahedral grids using a derivation that follows the 2-D case. The resulting equations are discussed in intuitive terms and an error analysis is performed. Our method is applied to a simple synthetic example and to a more complicated model based on the Voisey's Bay massive sulphide deposit in Labrador, Canada.

Key words: Numerical solutions; Computational seismology; Wave propagation.

1 INTRODUCTION

As discussed by Vidale (1988), first-arrival ray tracing can be problematic when shadow zones exist or where multiple paths between source and receiver are possible. Also, ray tracing becomes computationally impractical when many source–receiver pairs are considered. Calculating first arrival traveltimes via a finite difference approach on a discretized domain avoids problematic ray tracing.

Modelling of seismic traveltimes via propagation of wave fronts is governed by the Eikonal equation

$$\|\nabla t\|_2 = s, \tag{1}$$

where t is traveltime and s is the slowness, the inverse of velocity. Many authors have developed numerical methods for solving this equation on discretized domains. These methods work on a discretization of the subsurface where each cell in the grid is commonly assigned a constant slowness value; that is the approach taken here but, alternately, the slowness could change within each cell following some simple function. The solutions begin by initializing the traveltimes near-source and the traveltimes at grid nodes away from the source are then calculated using finite difference formulae. The various modelling approaches can be grouped by the way in which the solution front passes through the grid.

Vidale (1988) developed a solution for 2-D rectilinear grids in which the solution front marches away from a point source in a box shape. Vidale (1990) extended this to 3-D rectilinear grids, which was later updated by Podvin & Lecomte (1991). Expanding box schemes can be unstable when rays turn and violate causality rules (Kim & Cook 1999). The requirement of causality as defined by Vidale (1988) is that 'the time for the part of the ray path leading to a point must be known before the time of the point can be found'. Kim & Cook (1999) improved on the box marching instability issue by developing more accurate finite difference formulae and post-sweeping procedures for rectilinear grids. Schneider *et al.* (1992) incorporated a nonlinear interpolation and systematic mapping scheme to overcome the problem, and Hole & Zelt (1995) introduced a 1-D operator and a reverse propagation scheme to do so. Others took different routes that changed the marching strategy. Alkhalifah & Fomel (2001) developed a marching framework in spherical coordinates where the wave fronts are marched radially away from a point source. Qin *et al.* (1992) marched the solution front outwards on a regular grid in a way that roughly approximated the true wave fronts. Sethian (1996) developed a more efficient 'Fast Marching Method' (FMM) that advances wave fronts in a monotonic manner, thereby building causality directly into the marching scheme. The FMM solution fronts (i.e. the interface between grid nodes with traveltimes assigned and those without) then closely mirror the seismic wave fronts.

We choose to work with unstructured grids instead of rectilinear grids because the former allow for efficient generation of complicated subsurface geometries, such as those often encountered in hard-rock environments. This becomes important when one wishes to incorporate prior information into forward or inverse modelling investigations. Also, unstructured grids can significantly reduce the problem size involved in forward and inverse calculations compared to rectilinear grids by easily increasing cell volumes in particular regions of the subsurface while avoiding large aspect ratios of cell dimensions, which can produce modelling instability for some numerical solutions.

Criticism of the FMM approach includes that it is more expensive than the box marching equivalent and it cannot be easily modified to achieve high-order accuracy (Kim & Cook 1999),

although Sethian & Popovici (1999) suggest that use of a higher-order finite-difference approximation should be possible. These issues are irrelevant, however, when moving to unstructured grids where box marching is no longer applicable and the FMM becomes the marching scheme of choice.

An obvious limitation of the FMM, and indeed any marching finite-difference Eikonal solver, is that it is only able to produce the first-arrival solution. In applications such as seismic reflection imaging in complex media, the first-arrival solution may not be adequate (see Geoltrain & Brac 1993). To calculate multiple arrivals, one can perform computations in the phase space as do Fomel & Sethian (2002). Rawlinson & Sambridge (2004b) and de Kool *et al.* (2006) calculate multiple arrivals in layered media by reinitializing the FMM solution at reflective layer boundaries, thereby calculating multiple reflection and transmission phases. Another limitation is the assumption of isotropic velocity. An extension to anisotropic media, on unstructured grids, is provided by the ordered upwind methods of Sethian & Vladimirsky (2001) and Sethian & Vladimirsky (2003) (see also Sethian & Vladimirsky 2000).

Theory for the FMM and related level set methods is thoroughly covered in Sethian (1999b). The FMM provides a method for solving the Eikonal equation and thereby determining the propagation of first-arrival seismic wave fronts through a given slowness distribution. Initial work focussed on regular rectilinear 2-D grids (Sethian 1996). Sethian & Popovici (1999) extended the methods to similarly structured 3-D grids. Kimmel & Sethian (1998) developed an extension to unstructured 2-D triangular grids which is also covered in Sethian (1999a) and Rawlinson & Sambridge (2004a). Fomel (1997) also extended the methods to unstructured 2-D triangular grids, arriving at an equivalent result via a different formulation of the problem.

There has been some work using unstructured tetrahedral grids for seismic tomography, where rays are traced through 3-D models of Delaunay tetrahedral cells. For example, see Sambridge & Gudmundsson (1998) and Sambridge & Faletič (2003). Sambridge & Rawlinson (2005) outline some of the non-trivial book-keeping practicalities and other implementation issues involved when using unstructured tetrahedral grids in seismic modelling. Several authors have indicated the possibility of an extension of the FMM to unstructured tetrahedral grids: Fomel (1997), Rawlinson & Sambridge (2004a) and Rawlinson & Sambridge (2004b). However, the FMM has yet to be extended to these types of grids.

In this paper, we focus on the local update (finite difference stencil) required within the FMM solution for unstructured 3-D tetrahedral grids. The remainder of the FMM solution follows similar algorithmic details to other authors mentioned earlier so for brevity we provide only a brief summary below. We then provide an overview of the details of the local update on 2-D triangular grids. This is then extended to 3-D tetrahedral grids, followed by error analysis and two test scenarios. Our intention is to use our FMM solution as the forward solver within an inversion algorithm that works on unstructured grids, and we frame our concluding discussion based around that application.

2 SUMMARY OF THE FAST MARCHING METHOD

Consider the section of a regular rectilinear 2-D grid represented in Fig. 1. There are several methods for initializing the FMM solution. Our choice is to assume that the slowness of the medium is homogeneous in the local vicinity of the point source. We define an
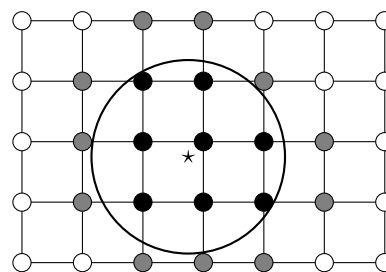
Figure 1. A section of a regular rectilinear 2-D grid on which an FMM solution is being initialized around a point source. Grid nodes are represented as small circles with thin connecting lines indicating the boundaries between grid cells. A seismic source is represented as a star and a large thick circle is drawn with the source at its centre; grid nodes within the circle are filled black and grid nodes immediately connected to nodes inside the circle are filled grey.
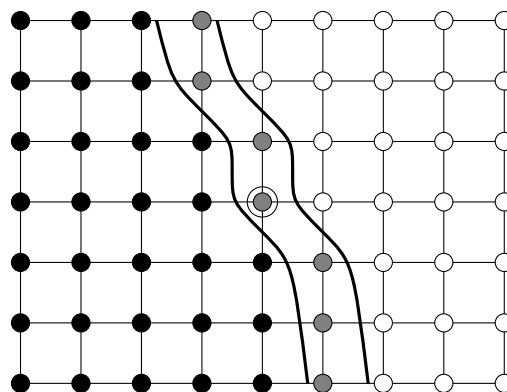

Figure 2. A section of a regular rectilinear 2-D grid through which an FMM solution is progressing. Grid nodes are represented as circles with thin connecting lines indicating the boundaries between grid cells. Upwind nodes are filled black, downwind nodes that are 'close' are filled grey, and downwind nodes that are 'far' are filled white. The central node is circled for referencing in the text. Two parallel thick lines represent either side of a narrow band of 'close' nodes.

initialization radius and calculate the traveltime at any nodes within that radius by multiplication of the local homogeneous slowness by the distance from the node to the source. Nodes can be specified as being either 'upwind' or 'downwind' from the solution front. Immediately after initialization, the large circle in Fig. 1 representing the initialization radius can be thought of as the solution front. Any nodes inside this radius are upwind and all other nodes are downwind from the solution front.

Now consider Fig. 2, which captures the FMM solution in part of the grid at a later stage. The downwind nodes are further categorized into a set of 'close' nodes immediately connected to upwind nodes, and a set of 'far' nodes not immediately connected to upwind nodes. Upwind nodes have firm traveltime values that cannot be altered at a later stage in the FMM solution. The traveltimes at the close downwind nodes are calculated based on the traveltimes at their neighbouring upwind nodes. Those calculations are referred to as local traveltime updates. For any particular close node, there may be several possible local update calculations. For example, for the circled close node in Fig. 2, the local update can be calculated through either of the two cells on its immediate left. The FMM calculates first arrivals so the actual traveltime taken by this node is the minimum of all those calculated through the local updates.

Once all the local traveltime updates are calculated for the close nodes, they define a narrow band of trial nodes that could be moved
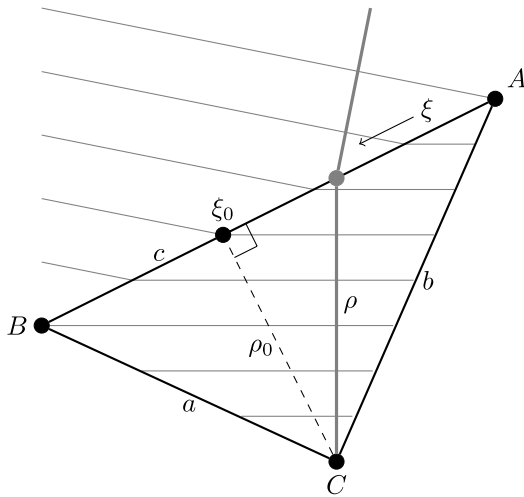
Figure 3. A geometrical scheme for the traveltime updating procedure in 2-D, adapted from Fomel (1997). A triangular cell lies between three nodes A, B and C. Linear wave fronts are drawn as thin grey lines. A traversing ray hitting node C is drawn as a thick grey line perpendicular to the wave fronts.

into the set of upwind nodes. The FMM moves the solution front forward monotonically. To do so, only the close node with the smallest traveltime is chosen to become an upwind node. Afterwards, any downwind nodes that were originally 'far' but are now connected to the new upwind node are added to the set of 'close' nodes. The procedure repeats until all nodes in the grid are upwind. The FMM is so-called 'fast' due to the use of an efficient heap sort strategy for determining which close node in the narrow band has the smallest traveltime.

A common approach is for the local traveltime updates to assume linear wave fronts (planar in 3-D) at the scale of the grid cells. The updates and this assumption are discussed in more detail in the following sections. The linear wave front assumption leads to first-order modelling accuracy. Although higher-order accuracy can be obtained, it complicates the numerical methods and we choose to follow the simplest path in this first attempt at developing a solution to the Eikonal equation on 3-D unstructured grids. When close to a point source, wave fronts will have a circular character (spherical in 3-D) and the assumption of locally linear wave fronts falls apart. The assumption will be more appropriate as the waves move further from the source. Hence, by increasing our initialization radius, we can reduce errors associated with the assumption of linear wave fronts in the local updates. An analysis of this source of error is provided in Section 5.

3 THE LOCAL TRAVELTIME UPDATE ON A 2-D TRIANGULAR GRID

3.1 Solution via Fermat's principle

Here we follow the procedure of Fomel (1997), although we perform a slightly different derivation and we provide additional intuitive comments on the meaning of some equations and mathematical quantities derived. Refer to Fig. 3 in the following discussion. The traveltimes at nodes A and B are t_A and t_B respectively, and are treated as known quantities calculated at previous stages in the FMM solution. The problem is to calculate a value for t_C, the traveltime at the remaining node C. The common assumption is made that the

wave fronts travelling through the cell are linear such that any rays travelling through the cell are also linear.

ξ is a normalized distance along the line segment from node A to node B (line AB), and ρ is the distance from node C to a point at ξ on line AB. ξ_0 is the normalized projection of node C onto line AB, and ρ_0 is the length of the normal from node C to the point at ξ_0. We can then write

$$
\begin{aligned}
t_C(\xi) &= t(\xi) + s\rho \\
&= t_A + u\xi + s\sqrt{c^2(\xi - \xi_0)^2 + \rho_0^2},
\end{aligned}
\tag{2}
$$

where $u = t_B - t_A$, c is the length of line AB, and s is the homogeneous slowness of the triangular cell. The term $t(\xi) = t_A + u\xi$ is the linearly interpolated traveltime at a point at ξ on line AB. The term $s\rho$ is the traveltime for the path from that point to node C, calculated as slowness multiplied by distance. That distance is calculated using Pythagoras' theorem applied to the right triangle connecting points C, ξ_0 and ξ.

Fomel (1997) invoked Fermat's principle which states that the ray to C should correspond to a local traveltime minimum. This equates to seeking a value for ξ that minimizes the traveltime through the cell, and therefore minimizes eq. (2). To solve, we first substitute $\tilde{\xi} = \xi - \xi_0$ into eq. (2) to give

$$
t_C(\tilde{\xi}) = t_A + u(\tilde{\xi} + \xi_0) + s\sqrt{c^2\tilde{\xi}^2 + \rho_0^2}.
\tag{3}
$$

We take the derivative of eq. (3) with respect to ξ and set to zero,

$$
\frac{dt_c}{d\xi} = \frac{dt_c}{d\tilde{\xi}} = u + sc^2\tilde{\xi}\left(c^2\tilde{\xi}^2 + \rho_0^2\right)^{-1/2} = 0,
\tag{4}
$$

which yields

$$
\tilde{\xi} = \pm w^{-1}c^{-1}u\rho_0
\tag{5}
$$

where we have defined

$$
w^2 = s^2c^2 - u^2 \geq 0
\tag{6}
$$

(see Section 3.3 for more on the $w^2 \geq 0$ requirement). Eq. (4) also indicates the equality

$$
\rho = -sc^2u^{-1}\tilde{\xi} = \mp scw^{-1}\rho_0.
\tag{7}
$$

We are interested in the value of $\tilde{\xi}$ in eq. (5) that minimizes t_C in eq. (3). If we specify that $t_B > t_A$ such that $u > 0$ then by considering the term $u(\tilde{\xi} + \xi_0)$ in eq. (3), the negative root in eq. (5) will provide the minimum solution. Hence, we have

$$
\xi = \xi_0 - w^{-1}c^{-1}u\rho_0,
\tag{8}
$$

$$
\rho = scw^{-1}\rho_0,
\tag{9}
$$

and substituting back into eq. (2) yields the simple expression

$$
t_C = t_A + u\xi_0 + wc^{-1}\rho_0.
\tag{10}
$$

Both eqs (8) and (10) are equivalent to those derived by Fomel (1997) but we have introduced the quantity w which we discuss further in Section 3.3.

3.2 The first-arrival local update

The traveltime in eq. (10) corresponds to a wave transmitted through the cell (and possibly refracted when passing across line AB from one cell to the next). The FMM local update considers both the transmitted wave traveltime defined by eq. (10) and traveltimes that

can be attributed to the phenomenon of head waves travelling along the sides AC and BC (Podvin & Lecomte 1991):

$$t_C = \min(t_A + u\xi_0 + wc^{-1}\rho_0, \ t_A + sb, \ t_B + sa). \tag{11}$$

However, the transmitted wave traveltime is only accepted as a valid option if the solution comes 'from within' the triangular cell. This means that 'the gradient of the solution at a grid point should point into the triangle from which it is updated' (Kimmel & Sethian 1998). In other words, the ray that traverses to node C should travel through the cell, and therefore should intersect the AB face. With the approach of Fomel (1997), this can be determined simply by testing whether $0 < \xi < 1$. When the solution is not from within the cell, we update t_C using the head wave traveltimes only:

$$t_C = \min(t_A + sb, \ t_B + sa). \tag{12}$$

3.3 Existence of a real, monotonic solution

A numerically problematic value of $w^2 < 0$ corresponds to a situation where the traveltime difference u between nodes A and B is larger than the time sc that it would take to travel along line AB at slowness s. There is then no possible orientation for linear wave fronts that is consistent with the parameters involved. This can occur when wave fronts travelling through the grid converge, and in this situation we again update t_C using the head wave traveltimes only as in eq. (12).

Finally, we mention that, as discussed in Kimmel & Sethian (1998), the solution above requires a non-obtuse triangulation 'so that any front entering the side of a triangle has two points to provide values before the third is computed.' This requirement ensures that the FMM wave front marching is performed in a monotonic manner, with each new traveltime calculated being later than those already determined. Consider updating the traveltime at node C from those at nodes A and B in the diagram in Fig. 4. wave fronts oriented such that rays travelling to C pass through the white region will yield solutions with t_C larger than t_A and t_B. However, wave fronts oriented such that rays travelling to C pass through the black region will yield solutions with t_C between t_A and t_B (this is the situation illustrated in Fig. 4). This results from the geometry of the obtuse triangle. If the angle at C is reduced below 90° the black region disappears. If the obtuse angle at C is increased, the black region will take up a higher proportion of the triangle's area. The larger the obtuse angle in a cell, the greater the chance of losing monotonicity when performing the local update in that cell. A similar situation
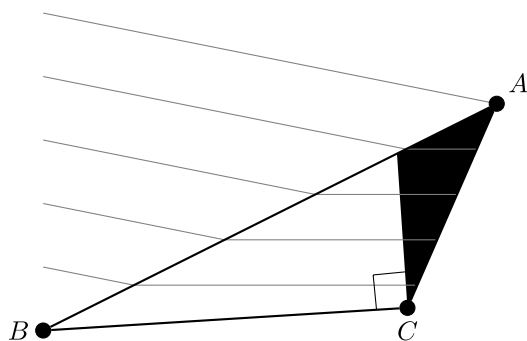
occurs in the 3-D case, for which the dihedral angles need to be below 90° to ensure monotonicity.
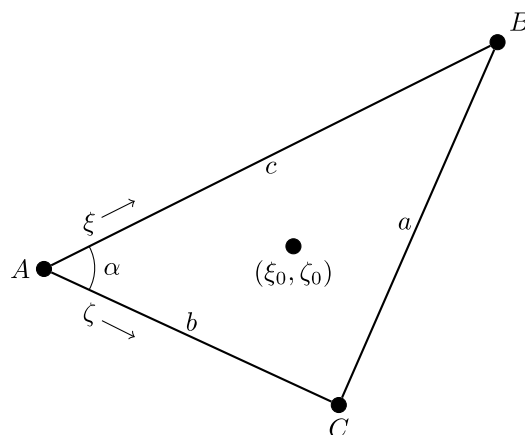
There are many unstructured mesh generators that have been developed and a thorough discussion of these is beyond the scope of this paper. To discretize our modelling domains we use two freely available programs, Triangle (Shewchuk 1996, 2002, 2003) for 2-D and TetGen (Si 2007; Si 2008a; Si 2008b; Si 2010; Si *et al.* 2010) for 3-D. Unfortunately, obtaining a nonobtuse triangularization or tetrahedralization with their algorithms is not always possible. Although this may be unacceptable for some modelling applications, if used within an inversion algorithm we may accept a relaxation in the requirement of monotonicity for two reasons. First, when obtuse angles exist, it is often possible for the local updates through the offending cells to maintain monotonicity, depending on the positioning and orientation of the cells compared to the FMM solution fronts. Secondly, unless rays turn sharply on a small scale in the locality of a cell with obtuse angle, then the non-monotonic FMM solution can be no worse than a box-type marching scheme. Because of the first-order accuracy of the local updates, the FMM solution on unstructured grids should be applied to adequately smooth models, for which rays will not turn sharply on a small scale.

4 EXTENSION TO A 3-D TETRAHEDRAL GRID

4.1 Solution via Fermat's principle

To extend the local update to 3-D on a grid of tetrahedral cells, now consider updating the traveltime at a fourth node, D, based on the traveltimes at the nodes belonging to the face opposite node D. Fig. 5 shows the triangular face opposite node D (face ABC). In an analogous manner to the 2-D scenario, wave fronts through the tetrahedral cell are assumed to be planar.

Our derivations are similar to the 2-D case and we define ξ as a normalized distance along line AB, ζ as a normalized distance along line AC, and ρ as the distance from node D to a point (ξ, ζ) on face *ABC*. We define vectors **c** and **b** that run along lines AB and AC respectively. The variables ξ and ζ are linear transforms of the Cartesian coordinates, and the vectors $\xi\mathbf{c}$ and $\zeta\mathbf{b}$ can be thought of as basis vectors for the plane defined by face ABC. Point (ξ_0, ζ_0) is the normalized projection of node D onto face ABC, and ρ_0 is the length of the normal from node D to the point (ξ_0, ζ_0). We can

Figure 4. A triangular cell lies between three nodes A, B and C. The angle ACB is obtuse. The cell is divided into two sections coloured white and black. The white section forms a right triangle with right angle at C. Linear wave fronts are drawn as thin grey lines.

Figure 5. A single face of a tetrahedron opposite a fourth vertex D.

now write

$$t_D(\xi, \zeta) = t(\xi, \zeta) + s\rho$$
$$= t_A + u\xi + v\zeta + s\rho, \tag{13}$$

where $u = t_B - t_A$, $v = t_C - t_A$ and s is the slowness of the tetrahedral cell. As in the 2-D case, the term $t(\xi, \zeta)$ is the linearly interpolated traveltime at a point (ξ, ζ) on face ABC, and the term $s\rho$ is the traveltime for the path from that point to node D.

We define $\tilde{\xi} = \xi - \xi_0$ and $\tilde{\zeta} = \zeta - \zeta_0$ such that the distance ρ is given by

$$\rho^2 = \|\tilde{\xi}\mathbf{c} + \tilde{\zeta}\mathbf{b}\|^2 + \rho_0^2$$
$$= (\tilde{\xi}\mathbf{c} + \tilde{\zeta}\mathbf{b})^T(\tilde{\xi}\mathbf{c} + \tilde{\zeta}\mathbf{b}) + \rho_0^2$$
$$= \tilde{\xi}^2\mathbf{c}^T\mathbf{c} + \tilde{\zeta}^2\mathbf{b}^T\mathbf{b} + 2\tilde{\xi}\tilde{\zeta}\mathbf{c}^T\mathbf{b} + \rho_0^2$$
$$= c^2\tilde{\xi}^2 + b^2\tilde{\zeta}^2 + 2d^2\tilde{\xi}\tilde{\zeta} + \rho_0^2 \tag{14}$$

where we have defined

$$d^2 = \mathbf{c}^T\mathbf{b} = cb\cos\alpha \tag{15}$$

and α is the angle at node A between the two vectors $\mathbf{c}$ and $\mathbf{b}$. The norm term in eq. (14) is the distance between points (ξ, ζ) and (ξ_0, ζ_0) on face ABC.

Again, we invoke Fermat's principle and take the derivative of $t_D(\tilde{\xi}, \tilde{\zeta})$ with respect to both $\tilde{\xi}$ and $\tilde{\zeta}$:

$$\frac{dt_D(\tilde{\xi}, \tilde{\zeta})}{d\tilde{\xi}} = \frac{d}{d\tilde{\xi}}\left(t_A + u(\tilde{\xi} + \xi_0) + v(\tilde{\zeta} + \zeta_0) + s\rho(\tilde{\xi}, \tilde{\zeta})\right)$$
$$= u + s\rho^{-1}(c^2\tilde{\xi} + d^2\tilde{\zeta}) \tag{16}$$

and similarly

$$\frac{dt_D(\tilde{\xi}, \tilde{\zeta})}{d\tilde{\zeta}} = v + s\rho^{-1}(b^2\tilde{\zeta} + d^2\tilde{\xi}). \tag{17}$$

Setting those derivatives to zero and rearranging gives two equations in two unknowns,

$$u^{-1}(c^2\tilde{\xi} + d^2\tilde{\zeta}) = -s^{-1}\rho(\tilde{\xi}, \tilde{\zeta}) \tag{18a}$$

$$v^{-1}(b^2\tilde{\zeta} + d^2\tilde{\xi}) = -s^{-1}\rho(\tilde{\xi}, \tilde{\zeta}). \tag{18b}$$

We solve by setting the two left-hand sides equal and rearranging to obtain

$$\tilde{\xi} = \left(\frac{ub^2 - vd^2}{vc^2 - ud^2}\right)\tilde{\zeta} = \frac{\beta}{\gamma}\tilde{\zeta} = \eta\tilde{\zeta}, \tag{19}$$

where we have defined the new quantities β, γ and η. Substituting $\tilde{\xi} = \eta\tilde{\zeta}$ into eq. (18a) and solving for $\tilde{\zeta}$ gives

$$\tilde{\zeta}^2 = \frac{u^2\rho_0^2}{s^2(c^2\eta + d^2)^2 - u^2((c^2\eta + d^2)\eta + (b^2 + d^2\eta))}. \tag{20}$$

We can simplify eq. (20) using the identities

$$c^2\eta + d^2 = u\varphi^2\gamma^{-1} \tag{21a}$$

$$d^2\eta + b^2 = v\varphi^2\gamma^{-1} \tag{21b}$$

which provide

$$\tilde{\xi} = -|\beta|\varphi^{-1}\tilde{w}^{-1}\rho_0 \tag{22a}$$

$$\tilde{\zeta} = -|\gamma|\varphi^{-1}\tilde{w}^{-1}\rho_0 \tag{22b}$$

where we have defined the new quantities

$$\varphi = cb\sin\alpha \tag{23a}$$

$$\tilde{w}^2 = s^2\varphi^2 - u^2b^2 - v^2c^2 + 2uvd^2. \tag{23b}$$

The negative signs in eq. (22) come from a similar argument to that which lead us to take the negative root in eq. (5). As in the 2-D case, we require $\tilde{w}^2 \geq 0$ which we discuss further in Section 4.3.

From eq. (18a) we have

$$\rho = -su^{-1}(c^2\tilde{\xi} + d^2\tilde{\zeta})$$
$$= -s\varphi^2\gamma^{-1}\tilde{\zeta}. \tag{24}$$

and eq. (13) now provides

$$t_D = t_A + u\xi_0 + v\zeta_0 + \tilde{w}\varphi^{-1}\rho_0, \tag{25}$$

a result remarkably similar to the 2-D case.

4.2 The first-arrival local update

Recall that in the 2-D case, the FMM local update generally considers the transmitted wave traveltime defined in eq. (10) and two traveltimes associated with travel along cell edges. In the 3-D case, we must consider six traveltimes in addition to the transmitted wave traveltime. Three of these travel along the linear edge elements of the tetrahedron and are calculated as

$$t_A + s\|AD\| \;,\; t_B + s\|BD\| \;,\; t_C + s\|CD\|, \tag{26}$$

where $\|AD\|$ is the distance from node A to node D (with similar definitions for $\|BD\|$ and $\|CD\|$). The physical interpretation of these traversals is that of diffraction (Podvin & Lecomte 1991). The remaining three waves travel along the triangular face elements of the tetrahedron that connect to node D and are interpreted as head waves. Those head wave traveltimes can be calculated by reducing each triangular face to the 2-D scenario in Section 3.

Again, the transmitted wave traveltime in eq. (25) is only accepted as a valid option if the solution comes from within the tetrahedral cell, which can be determined simply by testing whether the following are all true:

$$0 < \xi < 1, \tag{27a}$$

$$0 < \zeta < 1, \tag{27b}$$

$$0 < \xi + \zeta < 1. \tag{27c}$$

The same is true of the three head waves travelling along the triangular face elements.

4.3 Existence of a real solution

In eq. (22), we introduced the quantity $\tilde{w}$. A similar quantity w appeared in the 2-D case. Here we seek an intuitive understanding of what $\tilde{w}$ represents. To begin, consider the traveltime gradient ∇t in the plane defined by ABC, which we write as

$$\mathbf{p} = p_c\hat{\mathbf{c}} + p_b\hat{\mathbf{b}}, \tag{28}$$

Table 1. Coordinates that define a regular tetrahedron with centroid at the origin.

Node	x	y	z
A	0.943	0.000	−0.333
B	−0.471	0.816	−0.333
C	−0.471	−0.816	−0.333
D	0.000	0.000	1.000
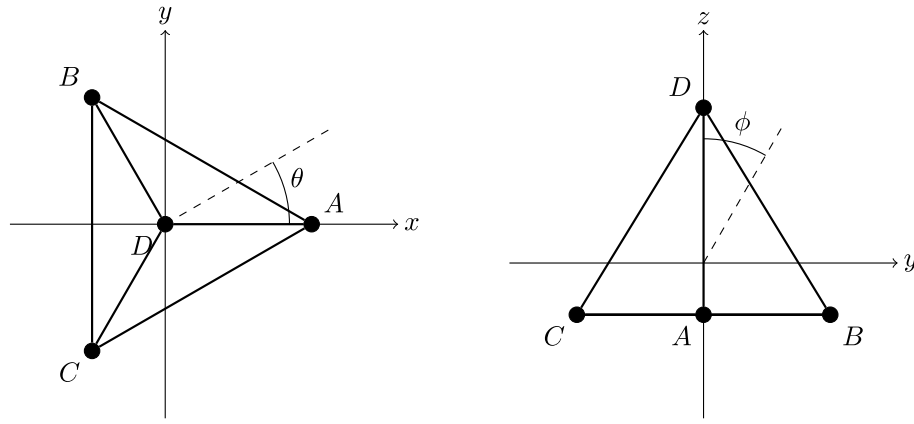
Figure 6. The tetrahedron defined in Table 1 as viewed from the $+z$ (left) and $+x$ (right) directions. We define an azimuthal angle θ and a polar angle ϕ as illustrated.

where $\hat{\mathbf{c}}$ and $\hat{\mathbf{b}}$ are unit vectors corresponding to the basis vectors $\mathbf{c}$ and $\mathbf{b}$. By taking the dot product of this gradient we can write two equations in two unknowns
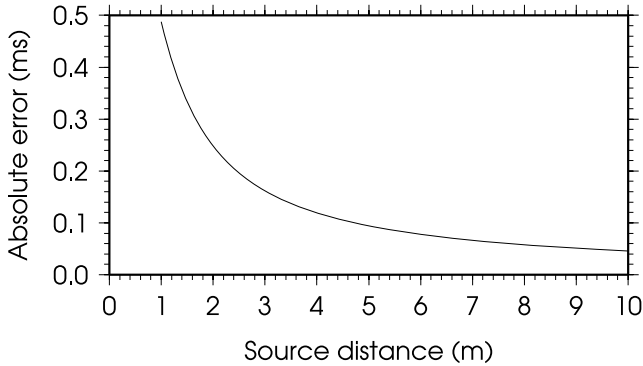
$$\mathbf{p} \cdot \mathbf{c} = p_c c + p_b c \cos \alpha = u, \tag{29a}$$

$$\mathbf{p} \cdot \mathbf{b} = p_b b + p_c b \cos \alpha = v, \tag{29b}$$

for which the solution is

$$p_c = \frac{ub - vc \cos \alpha}{cb \sin^2 \alpha}, \tag{30a}$$

$$p_b = \frac{vc - ub \cos \alpha}{cb \sin^2 \alpha}. \tag{30b}$$

Table 2. Maximum tetrahedral volumes supplied to TetGen, the resulting number of grid nodes and tetrahedral cells used to discretize a cube of 100 m dimensions, and the CPU computation time for the FMM solutions on those grids using a 2.53 GHz dual core machine.

Volume (m^3)	Nodes	Cells	Time (s)
1	307692	1889668	21.76
8	40441	236485	2.56
64	5627	30028	0.30
216	1803	8781	0.08

Table 3. Histogram information for obtuse dihedral angles contained in the meshes created by TetGen (see Table 2 for more information). Here we show percentages of cells with maximum dihedral angles within the indicated bins.

Volume (m^3)	$(90,100]°$	$(100,110]°$	$(110,120]°$	$(120,170]°$
1	27 per cent	19 per cent	12 per cent	19 per cent
8	27 per cent	19 per cent	13 per cent	19 per cent
64	26 per cent	19 per cent	13 per cent	19 per cent
216	27 per cent	19 per cent	13 per cent	20 per cent

Figure 7. Absolute error versus source distance for the FMM local update through the tetrahedral cell in Table 1 and Fig. 6 with $\theta = 0$ and $\phi = 180$.
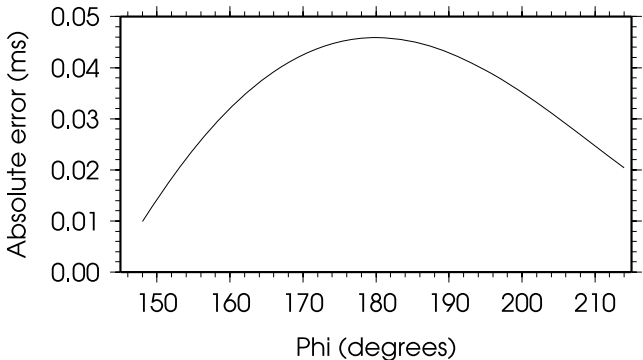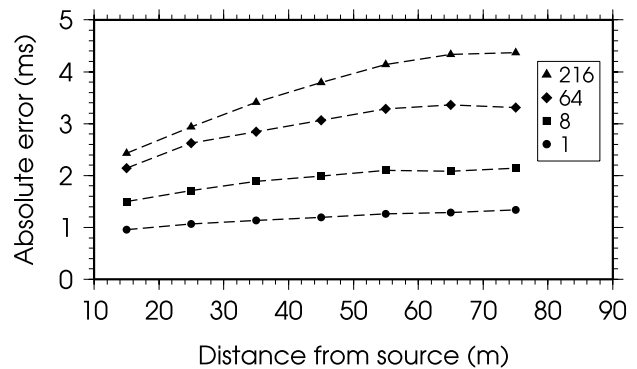

Figure 8. Absolute error versus ϕ for the FMM local update through the tetrahedral cell in Table 1 and Fig. 6 with $\theta = 0$ and source distance 10.0 m.

Figure 9. Absolute error versus nodal distance from source for four different discretizations. The distances are binned every 10 m and the maximum error is plotted for each bin (at the locations of the bin centres on the horizontal axis). The legend indicates maximum cell volumes in cubic metres.
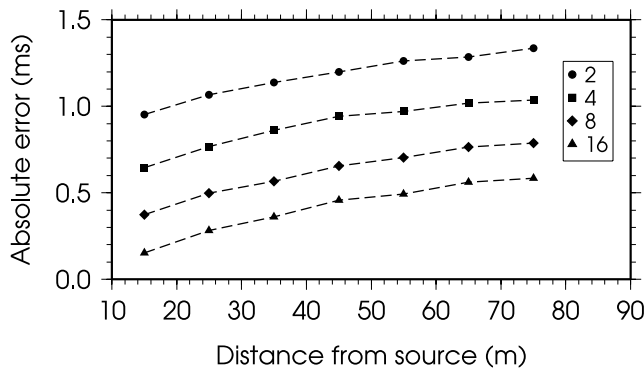
Figure 10. Absolute error versus nodal distance from source for four different initialization radii. The distances are binned every 10 m and the maximum error is plotted for each bin. The legend indicates initialization radii in metres.

We can now write

$$\|\mathbf{p}\|^2 = \mathbf{p}^T\mathbf{p} = p_c^2 + p_b^2 + 2p_c p_b \cos\alpha \qquad (31)$$

and substituting the result in eq. (30) gives

$$\|\mathbf{p}\|^2 = \frac{u^2 b^2 + v^2 c^2 - 2uvcb\cos\alpha}{c^2 b^2 \sin^2\alpha}. \qquad (32)$$

Comparing to eq. (23) we see that

$$\tilde{w}^2 = (s^2 - \|\mathbf{p}\|^2)\varphi^2. \qquad (33)$$

Hence, as in the 2-D case, a numerically problematic value of $\tilde{w}^2 < 0$ corresponds to a situation where the traveltimes at nodes A, B and C define a traveltime gradient magnitude across face ABC that is larger than the slowness s. There is then no possible orientation for planar wave fronts that is consistent with the parameters involved. Again, this can occur when wave fronts travelling through the grid converge, and in this situation we update t_D using the additional diffraction and head wave traveltimes only.
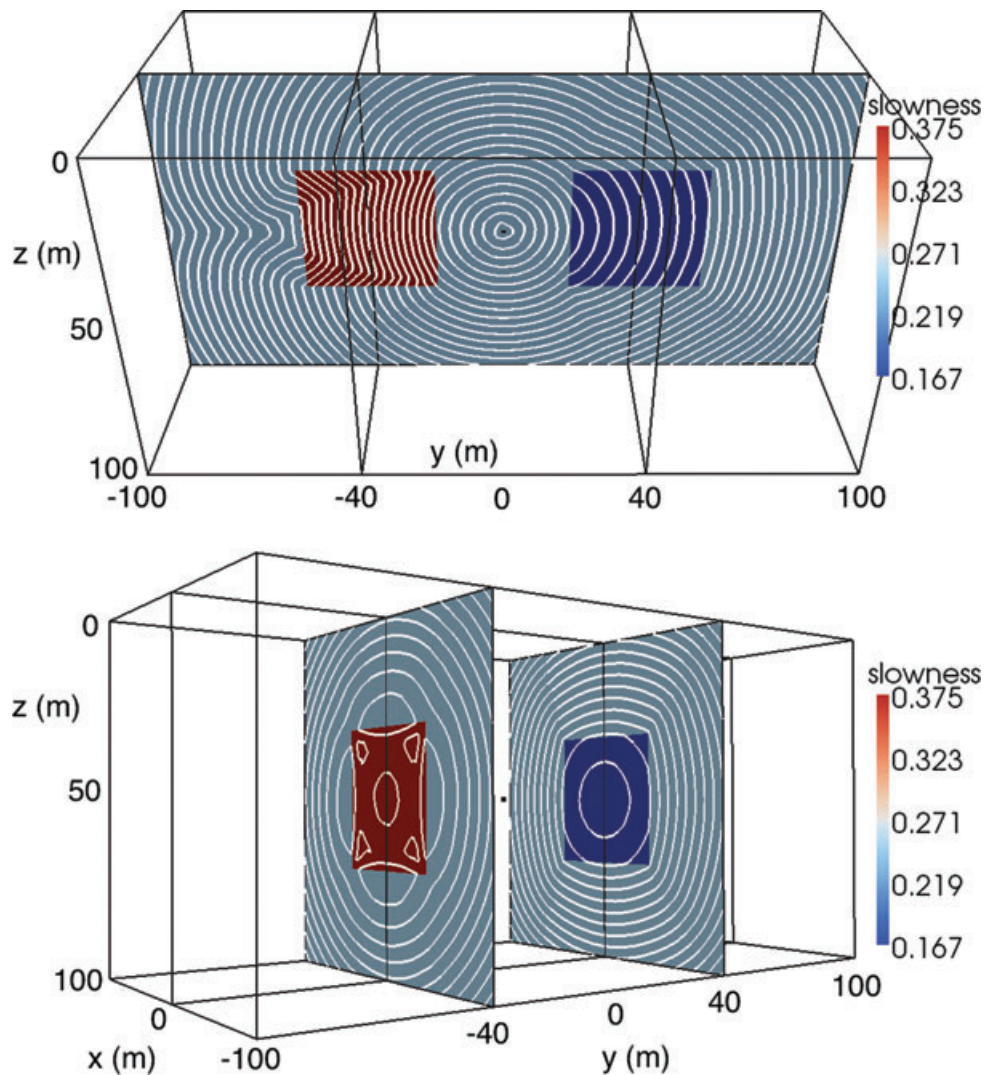
Figure 11. Vertical slices through the synthetic block model used to test our FMM solution for 3-D tetrahedral grids. Model slowness values are indicated by the colour scale (units are s km^{-1}). White contours are displayed at 0.8 ms intervals. The source in the centre of the model is displayed as a black dot. The outline of the modelling region and the locations of the slices are indicated in black.

5 ERROR ANALYSIS

5.1 Error in the local update

The major source of modelling error in our FMM solution on a 3-D tetrahedral grid relates to the assumption of planar wave fronts. For a point source, the wave fronts will be spherical in a homogeneous medium and can only be considered effectively planar on the scale of the tetrahedral cells at relatively large distances from the source. Here we investigate the error associated with this assumption during a local update on a tetrahedral cell using eq. (25).

We consider a regular tetrahedron for which each face is an equilateral triangle. One such tetrahedron, positioned with its centroid at the origin, will have nodes at the coordinates in Table 1. This tetrahedron is illustrated in Fig. 6.

We position a source at some distance away from the tetrahedron on the negative side of the z-axis and set the homogeneous slowness to $1.0\,\mathrm{s\,km^{-1}}$. We calculate the exact traveltime at all nodes by multiplying the distance of each node from the source by the slowness. We then calculate a second, approximate traveltime at node D from those at nodes A, B and C using eq. (25).

The first plot we present, Fig. 7, shows the absolute difference between the two traveltimes calculated at node D versus the distance of the source to the origin (the centroid of the tetrahedron). As expected, the error reduces as the distance from the source increases,

corresponding to an increased validity of the assumption of planar wave fronts.

For our second plot, Fig. 8, we allow the location of the source to move away from the z-axis while maintaining a constant distance of the source from the origin. We define a spherical coordinate system with θ the azimuthal angle from $+x$ towards $+y$ and ϕ the polar angle equal to zero along the $+z$ direction. With $\theta = 0$ and the source 10 m from the origin we plot the error in the local update as the angle ϕ sweeps across all angles that lead to a solution for the traveltime at node D such that the solution comes from within the tetrahedron, as discussed in Section 4.2. Different θ angles provide similar plots, with the largest errors occurring when the ϕ angle is close to $180°$ such that the incoming wave fronts are about parallel to face ABC.

The plots in Figs 7 and 8 are similar when irregular tetrahedra are considered, with or without obtuse dihedral angles. The plots indicate that the orientation of a tetrahedron with respect to the incoming wave fronts has far less effect on the FMM local update error than does the distance from the source.

5.2 Errors on a homogeneous grid

We now move on to investigate how the errors associated with the local updates combine as the FMM solution marches through the
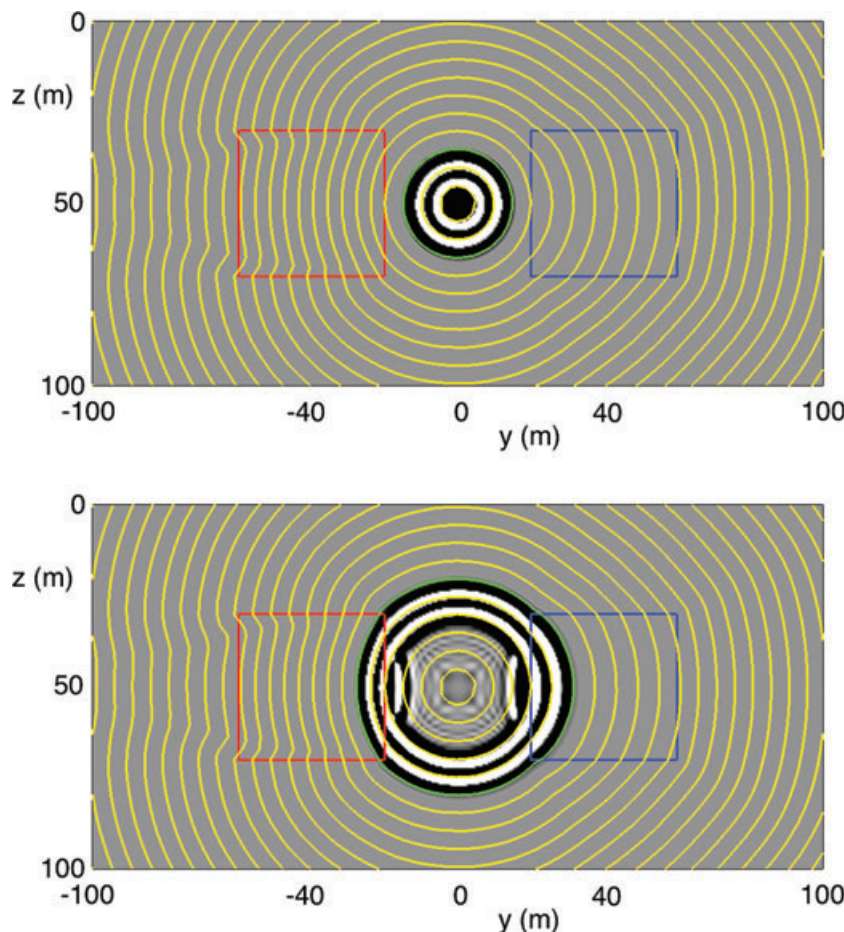
Figure 12. Vertical slices at $x = 0$ through the synthetic block model used to test our FMM solution for 3-D tetrahedral grids. The slow and fast blocks are outlined in red and blue, respectively. Yellow contours from the FMM solution are displayed at 1.0 ms intervals. Wave amplitudes from the E3D solution are plotted in greyscale with the contrast set high to easily identify the leading black wave. The E3D solutions at 3.0 and 6.0 ms are displayed at top and bottom, respectively. For each plot, the FMM contour at the relevant solution time is coloured green.

grid. To do so, we use TetGen to mesh a large cube with 100 m dimensions into many tetrahedral cells. We discretize using several values for the maximum tetrahedron volume supplied to TetGen as a meshing constraint. Table 2 shows the maximum volumes used and the resulting number of grid nodes and cells for each discretization. Table 3 shows histogram information for the obtuse dihedral angles contained in the meshes.

We place a source at the origin in the centre of the large homogeneous cube and for each discretization we calculate traveltimes at the grid nodes using the FMM solution and by multiplying the distance of each node from the source by the slowness (i.e. the exact solution). Again, we set the homogeneous slowness to 1.0 s km^{-1}. We initialize the traveltime grid only at the nodes directly surrounding the source (i.e. the minimum initialization radius available).

Fig. 9 shows the error in the FMM solution as it marches away from the source. Because there are so many nodes in each grid, we bin the nodes by their distances from the source every 10 m and we plot the maximum errors in each bin. As expected, Fig. 9 shows an increase in error with a decreasing level of discretization (grids with fewer, larger cells). It also indicates that for a given grid, the errors in the numerical FMM solution begin to level off with distance from the source. This is expected considering Fig. 7 which tells us that the local update errors reduce considerably away from the source. We emphasize here that we provide Fig. 9 to indicate the mentioned error trends; the absolute errors can be reduced by improving on the near-source initialization accuracy, as we show later.

Finally, we investigate the effect of the initialization radius on the error. We use the finest discretization above and use initialization radii of 2, 4, 8 and 16 m. Fig. 10 shows the error in the FMM solution as it marches away from the source, with the nodal distances again binned as before. The initialization radius shows an approximately logarithmic relationship with the error in this example, the error increasing linearly as the radius decreases every power of 2. To reduce this important source of error, the initialization radius should be made as large as possible. However, this requires a homogeneous near-source region. If heterogeneity exists near a source then the discretization in that region should be changed to use finer cells, as is performed in Rawlinson & Sambridge (2004b) as advocated by Kim & Cook (1999). This is one of the great advantages of using an unstructured discretization as finer cells can be added only where needed. If the receivers lie in a homogeneous region, another possible work-around would be to use the reciprocity principle to swap sources and receivers.

6 FMM SOLUTION EXAMPLES ON 3-D TETRAHEDRAL GRIDS

6.1 A simple block model

Here we show results for a simple model built from two blocks with anomalous slownesses of 0.375 and 0.167 s km^{-1} inside a background of 0.250 s km^{-1} (velocities of 2.67, 6.00 and 4.00 km s^{-1}, respectively). The modelling region has lateral dimensions of 100 m × 200 m and a depth of 100 m. The two blocks are cubes of dimension 40 m. The centres of the two blocks are separated by
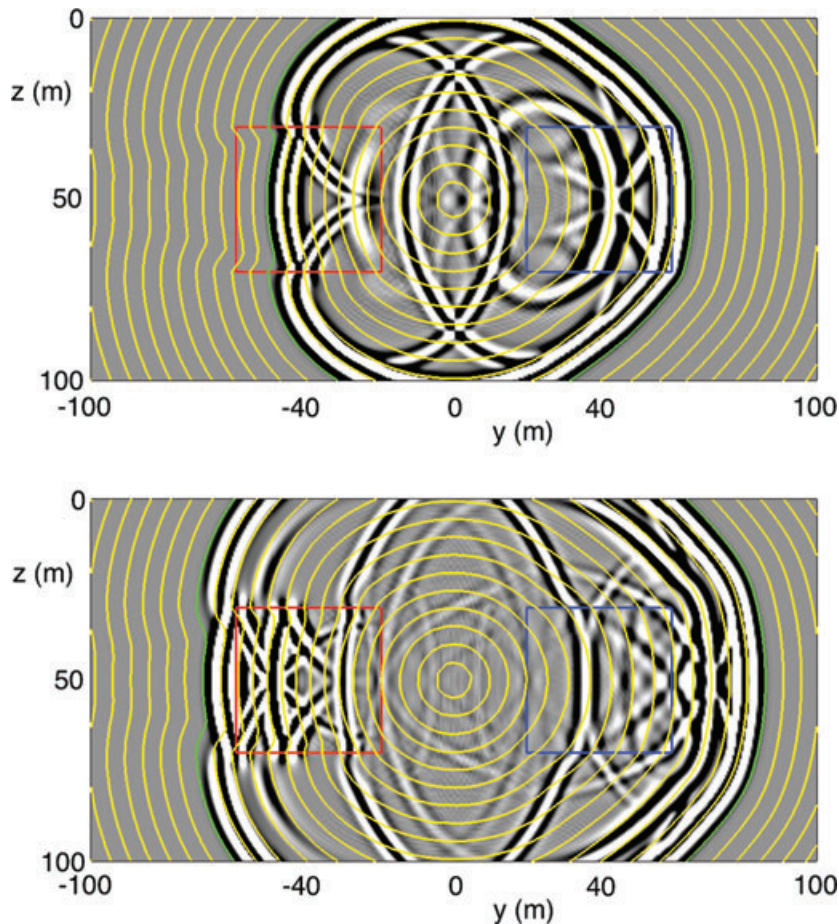
Figure 13. As in Fig. 12 but at times 12.0 and 16.0 ms at top and bottom, respectively.

80 m. A single source is placed in the centre of the model, the midpoint between the centres of the two blocks.

We discretize the model into a tetrahedral grid using TetGen, constraining the grid cells to have a maximum volume of 8 m^3. The resulting grid contains 79 987 nodes and 475 896 tetrahedral cells. The traveltimes at each node in the grid are calculated using the FMM with our local update procedure for tetrahedral cells.

Fig. 11 shows vertical slices through the model, bisecting both blocks along symmetry planes. Traveltime contours (isochrons) every 0.8 ms are displayed on the slices. As expected, wave fronts slow down (smaller separation between isochrons) as they travel through the slower part of the model, and they speed up (larger separation between isochrons) as they travel through the faster part of the model. Furthermore, refraction, diffraction and head wave effects are evident as the solution fronts pass across the boundaries between the different regions. The 3-D results are comparable to those we obtain via an FMM solution on similar 2-D scenarios.

We compare our solution against that obtained using the 3-D elastic seismic wave propagation program E3D (Larsen & Schultz 1995). The source for the E3D solution was a Ricker Wavelet with a centre frequency of 750.0 Hz, chosen to produce a wave front that is well enough localized to allow a comparison with our FMM solution. The spatial discretization for the E3D solution is a regular

rectilinear grid using cubic cells with dimensions of 0.25 m. The time steps for the solution are at 0.02 ms intervals. Modelling accuracy considerations lead to conditions on the spatial discretization and time stepping that depend on the source wavelength and model slowness values. Because of those considerations, the computational requirements of the E3D program and the computing power available to us, we have altered the slowness values to 0.250 and 0.167 s km^{-1} inside a background of 0.200 s km^{-1} for this comparison. This reduces the refraction, diffraction and head wave effects slightly. Figs 12 and 13 show the same vertical slice through the middle of the two blocks as seen at top in Fig. 11. The wave amplitudes from the E3D solution are plotted in greyscale with contours from our FMM solution overlaid. Our contours agree well with the leading waves in the elastic wave solution, although the amplitudes at later times are reduced on the left of the images due to diffraction effects associated with the slow block.

## 6.2 A model of the Voisey's Bay ovoid deposit

We now move on to a more complicated model, one that would be problematic to discretize on a rectilinear grid and is therefore representative of the types of Earth models that we are interested in dealing with. The Voisey's Bay nickel-copper–cobalt deposit in Labrador is considered to be one of the most important recent mineral discoveries in Canada. The physical property data indicate typical velocities of 4.4 km s^{-1} for the massive sulphide ore body,
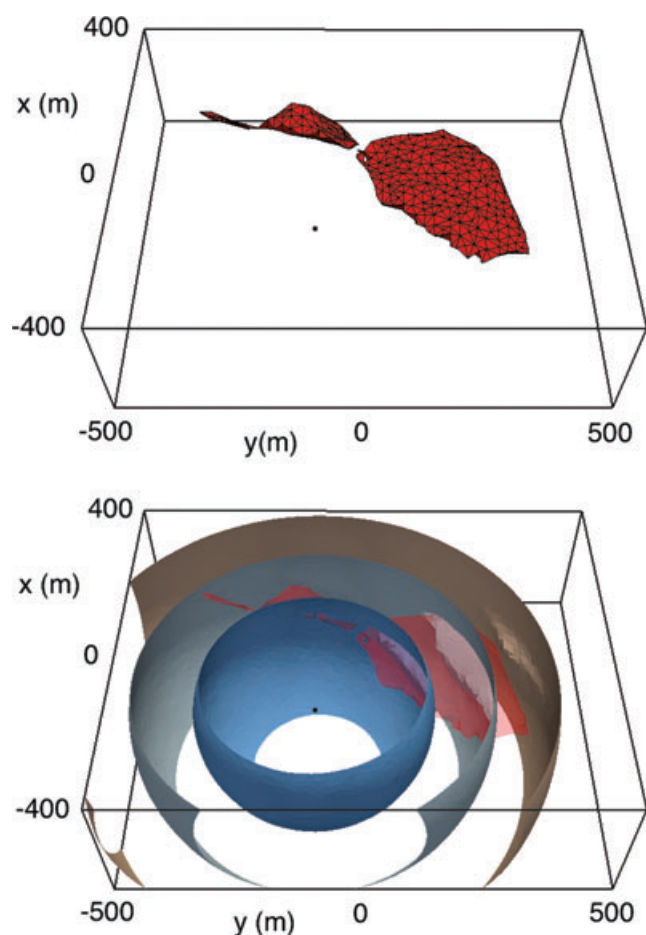
Figure 14. A perspective view of the 3-D Voisey's bay model, looking down from the south. At top, the ovoid surface is red with black cell edges to indicate the discretization. At bottom, the ovoid surface is transparent and three traveltime contours (non-red) have been added for times of 40, 60 and 80 ms. The location of the seismic source is indicated by a black dot.
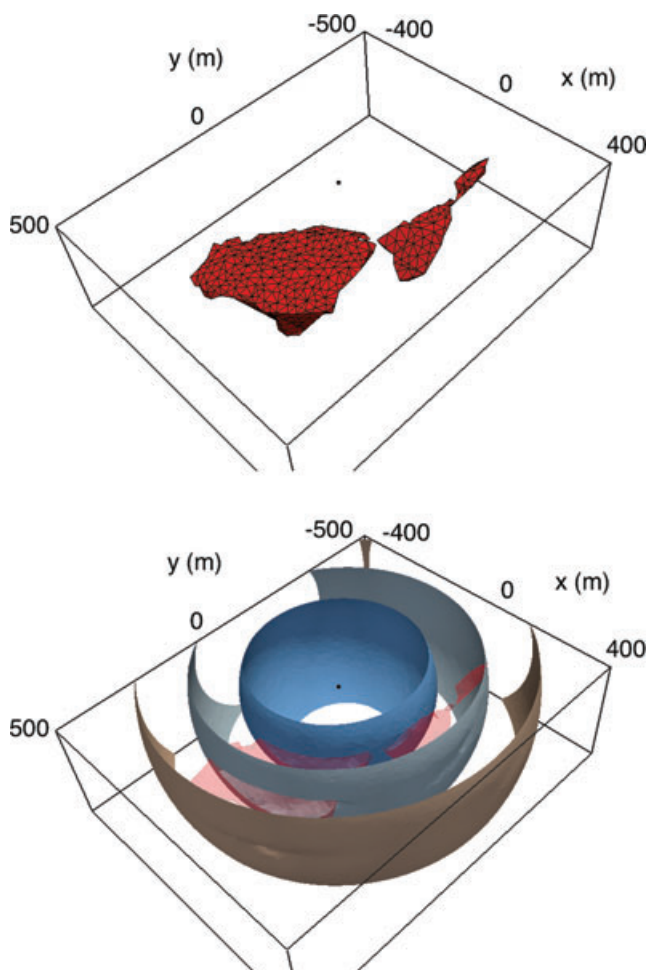
Figure 15. As in Fig. 14 but looking down from the northeast.
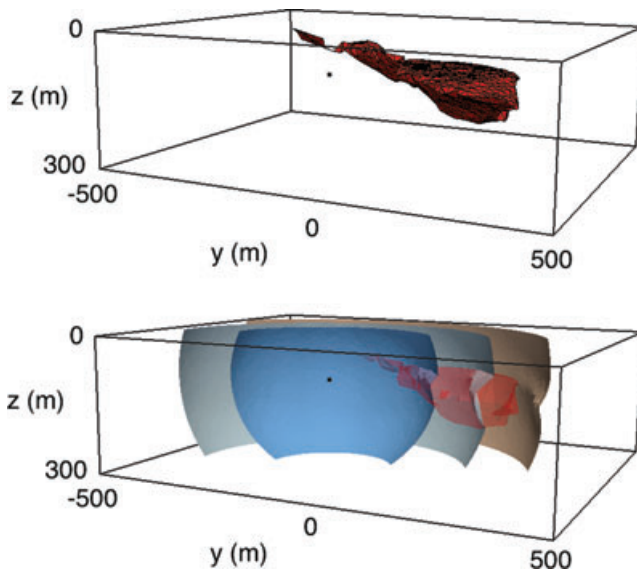
Figure 16. As in Fig. 14 but looking sideways from the south east. The traveltime contours have been clipped to better show depressions in their surfaces.

from herein referred to as the ovoid, and 6.1–6.5 km s^{-1} for the surrounding rock (Duff & Hurich 2006). A triangulated surface model for the ovoid has been generated from drillcore logging and can be used to constrain the meshing of our tetrahedral modelling grid.

Our modelling region has lateral dimensions of 800 m × 1000 m and a depth of 300 m. We discretize the ovoid model into a tetrahedral grid using the TetGen program, constraining the grid cells to have a maximum volume of 100 m^3. The resulting grid contains 75 602 nodes and 444 984 tetrahedral cells. Velocities used for the background and ovoid are 6.3 and 4.4 km s^{-1}, respectively (slowness values of 0.16 and 0.23 s km^{-1}, respectively). We use an initialization radius of 50 m.

Figs 14–16 show the ovoid surface and three isochron surfaces through the 3-D traveltime solution. The solution behaves as expected, with wave fronts slowing through the ovoid as evident from the depressions in the isochron surfaces.

7 DISCUSSION

We have extended the Fast Marching Method for use on unstructured 3-D tetrahedral grids by developing a local update for such grids. The update has many similarities to that developed by Fomel (1997) for unstructured 2-D triangular grids and makes intuitive sense. Our method has been tested numerically and the examples we have shown display the behaviours expected of seismic waves travelling through heterogeneous velocity distributions. An error analysis has been performed that provided results expected from consideration of the assumptions made within the FMM local update calculations. This analysis indicates some basic guidelines for designing grids when modelling accuracy is a concern.

We recognize that our approach is only first-order accurate, and worse if obtuse dihedral angles exist in the tetrahedral mesh. This work is an important first step in developing a more rigorous solution on 3-D unstructured grids. We hope that future work by ourselves or others will extend our methods to higher-order accuracy and to ameliorate the issue of obtuse dihedral angles.

Discretizing the subsurface with unstructured 2-D triangular and 3-D tetrahedral grids allows for efficient generation of complicated subsurface geometries that are difficult to represent with rectilinear grids. First-arrival seismic traveltimes can now be calculated for velocity models built on unstructured 3-D tetrahedral grids. Given a velocity model defined as a surface of tessellated triangles, one can use TetGen or other meshing software to generate a tetrahedral modelling mesh that is constrained by that surface. This is the procedure we have taken in the examples in this manuscript. The constraining surfaces could also define arbitrarily shaped reflectors, allowing reflection and transmission branches to be readily computed. If, instead, a velocity model is provided on a tetrahedral mesh, TetGen or other meshing software can be used to refine this mesh for modelling purposes, ensuring that the discretization is at the desired level within particular regions of the mesh. If velocity information is provided as densely sampled points within the modelling volume, a mesh can be generated using the methods of Rüger & Hale (2006), although TetGen is also capable of meshing this same information.

Our work opens the door to inversion of first-arrival data on unstructured 3-D grids for complicated, real-life scenarios. For such an application, errors present in the forward modelling must be kept small. The acceptability of the first-order accuracy can only be determined on a case-by-case basis. However, due to uncertainties inherent in survey data, and computing power limitations on the discretization used, the first-order modelling accuracy is expected to be acceptable in many cases.

REFERENCES

Alkhalifah, T. & Fomel, S., 2001. Implementing the fast marching eikonal solver: spherical versus cartesian coordinates, *Geophys. Prospect.,* **49**(2), 165–178.

de Kool, M., Rawlinson, N. & Sambridge, M., 2006. A practical grid-based method for tracking multiple refraction and reflection phases in three-dimensional heterogeneous media, *Geophys. J. Int.,* **167**(1), 253–270.

Duff, D. & Hurich, C.A., 2006. Physical property analysis, numerical and scale modeling for planning of seismic surveys: Voisey's bay, Labrador, in *SEG Expanded Abstracts*, Vol. 25, pp. 1343–1346.

Fomel, S., 1997. A variational formulation of the fast marching eikonal solver, in *SEP-95: Stanford Exploration Project*, pp. 127–147.

Fomel, S. & Sethian, J.A., 2002. Fast-phase space computation of multiple arrivals, *Proc. Natl. Acad. Sci. USA*, **99**(11), 7329–7334.

Geoltrain, S. & Brac, J., 1993. Can we image complex structures with first-arrival traveltime?, *Geophysics*, **58**(4), 564–575.

Hole, J.A. & Zelt, B.C., 1995. 3-D finite-difference reflection traveltimes, *Geophys. J. Int.,* **121**(2), 427–434.

Kim, S. & Cook, R., 1999. 3-D traveltime computation using second-order ENO scheme, *Geophysics*, **64**(6), 1867–1876.

Kimmel, R. & Sethian, J.A., 1998. Computing geodesic paths on manifolds, *Proc. Natl. Acad. Sci. USA*, **95**(15), 8431–8435.

Larsen, S.C. & Schultz, C.A., 1995. ELAS3D: 2D/3D elastic finite-difference wave propagation code, Technical Report UCRL-MA-121792, Lawrence Livermore National Laboratory, Livermore, CA.

Podvin, P. & Lecomte, I., 1991. Finite difference computation of traveltimes in very contrasted velocity models: a massively parallel approach and its associated tools, *Geophys. J. Int.,* **105**(1), 271–284.

Qin, F., Luo, Y., Olsen, K.B., Cai, W. & Schuster, G.T., 1992. Finite-difference solution of the eikonal equation along expanding wave fronts, *Geophysics*, **57**(3), 478–487.

Rawlinson, N. & Sambridge, M., 2004a. Wave front evolution in strongly heterogeneous layered media using the fast marching method, *Geophys. J. Int.,* **156**(3), 631–647.

Rawlinson, N. & Sambridge, M., 2004b. Multiple reflection and transmission phases in complex layered media using a multistage fast marching method, *Geophysics*, **69**(5), 1338–1350.

Rüger, A. & Hale, D., 2006. Meshing for velocity modeling and ray tracing in complex velocity fields, *Geophysics*, **71**(1), U1–U11.

Sambridge, M. & Faletič, R., 2003. Adaptive whole Earth tomography, *Geochem. Geophys. Geosyst.,* **4**(3), 1022, doi:10.1029/2001GC000213.

Sambridge, M. & Gudmundsson, O., 1998. Tomographic systems of equations with irregular cells, *J. geophys. Res.,* **103**(B1), 773–781.

Sambridge, M. & Rawlinson, N., 2005. Seismic tomography with irregular meshes, in *Seismic Earth: Array Analysis of Broadband Seismograms*, in Geophysical Monograph Series, Vol. 157, pp. 49–65, eds Lavender, A. & Nolet, G., AGU, Washington, D.C.

Schneider, W.A., Jr, Ranzinger, K.A., Balch, A.H. & Kruse, C., 1992. A dynamic programming approach to first arrival traveltime computation in media with arbitrary distributed velocities, *Geophysics*, **57**(1), 39–50.

Sethian, J.A., 1996. A fast marching level set method for monotonically advancing fronts, in *Proc. Natl. Acad. Sci. USA*, **93**, 1591–1595.

Sethian, J.A., 1999a. Fast marching methods, *SIAM Rev.,* **41**(2), 199–235.

Sethian, J.A., 1999b. Level Set methods and fast marching methods: evolving interfaces in computational geometry, fluid mechanics, computer vision and materials science. *Cambridge Monographs on Applied and Computational Mathematics*, Cambridge University Press, New York, NY.

Sethian, J.A. & Popovici, A.M., 1999. 3-D traveltime computation using the fast marching method, *Geophysics*, **64**(2), 516–523.

Sethian, J.A. & Vladimirsky, A., 2000. Fast methods for the Eikonal and related Hamilton-Jacobi equations on unstructured meshes, *Proc. Natl. Acad. Sci. USA*, **97**(11), 5699–5703.

Sethian, J.A. & Vladimirsky, A., 2001. Ordered upwind methods for static Hamilton-Jacobi equations, *Proc. Natl. Acad. Sci. USA*, **98**(20), 11069–11074.

Sethian, J.A. & Vladimirsky, A., 2003. Ordered upwind methods for static Hamilton-Jacobi equations: theory and algorithms, *SIAM J. Numer. Anal.,* **41**(1), 325–363.

Shewchuk, J.R., 1996. Triangle: engineering a 2D quality mesh generator and delaunay triangulator. in *Applied Computational Geometry: Towards Geometric Engineering*, Vol. 1148 of Lecture Notes in Computer Science, pp. 203–222, eds Lin, M.C. & Manocha, D., Springer-Verlag, Berlin.

Shewchuk, J.R., 2002. Delaunay refinement algorithms for triangular mesh generation, *Comput. Geometry: Theory Appl.,* **22**(1–3), 21–74.

Shewchuk, J.R., 2003. Triangle: a two-dimensional quality mesh generator and delaunay triangulator, http://www.cs.cmu.edu/~quake/triangle.html (last accessed 2010 November).

Si, H., 2007. Tetgen: A quality tetrahedral mesh generator and a 3d delaunay triangulator, http://tetgen.berlios.de (last accessed 2010 November).

Si, H., 2008a. Three dimensional boundary conforming Delaunay mesh generation, *PhD thesis*, TU Berlin.

Si, H., 2008b. Adaptive tetrahedral mesh generation by constrained Delaunay refinement, *Int. J. Numerical Methods Eng.*, **75**(7), 856–880.

Si, H., 2010. Constrained delaunay tetrahedral mesh generation and refinement, *Finite elements in Analysis and Design*, **46**(1–2), 33–46.

Si, H., Fuhrmann, J. & Gärtner, K., 2010. Boundary conforming Delaunay mesh generation, *Computational Mathematics and Mathematical Physics*, **50**(1), 38–53.

Vidale, J., 1988. Finite-difference calculation of traveltimes, *Bull. seism. Soc. Am.,* **78**(6), 2062–2076.

Vidale, J.E., 1990. Finite-difference calculation of traveltimes in three dimensions, *Geophysics*, **55**(5), 521–526.